Peng, X., and Zornberg, J.G. (2016). "Evaluation of Load Transfer in Triaxial Geogrids using Transparent Soil." Proceedings of the *3rd Pan-American Conference on Geosynthetics*, Miami, Florida, 10-13 April, Vol. 2, pp. 1520-1531.

EVALUATION OF LOAD TRANSFER IN TRIAXIAL GEOGRIDS USING TRANSPARENT SOIL

Xin Peng and Jorge G. Zornberg, Department of Civil, Architectural and Environmental Engineering, The University of Texas at Austin, Austin, Texas, USA

ABSTRACT

The design of reinforced soil retaining structures and of reinforced pavements requires proper evaluation of the load-transfer mechanisms between soil particles and reinforcement. In the case of geogrid reinforcements, the passive resistance mobilized on transverse (or diagonal) ribs is an important factor that defines the mechanical response for both: (1) the ultimate pullout strength, and (2) the in-plane stiffness (under small displacements) of the reinforced system. In this paper, a new experimental testing program involving the use of the transparent soil (a mixture of fused quartz and mineral oils) was conducted to visualize the load transfer of diagonal ribs of triaxial geogrids. Specifically, small-scale soil-geosynthetic interaction tests involving geogrid samples as well as modified individual-rib samples were conducted. High-definition cameras were utilized to track the movement of junctions and deflections in the diagonal ribs. Image-processing techniques were used to obtain the displacements of geogrid individual components (junctions and ribs) from digital images. The continuous deformations of diagonal ribs, which can provide the basis for analytic modeling for soil-geogrid load transfer mechanisms, also could be collected via these image-processing techniques.

1. INTRODUCTION

The mechanical behavior of geogrid-reinforced soil retaining structures and of geogrid-reinforced pavements are significantly affected by the load-transfer mechanisms between soil particles and reinforcement. A number of experimental and numerical studies involving pullout loading tests have been reported in the technical literature (Wilson-Fahmy and Koerner 1993; Ochiai et al. 1996; Alagiyawanna et al. 2001; Teixeira et al. 2007; Sieira et al. 2009; Tran et al. 2013.). In these studies, the pullout resistance is typically considered to result from two contributions: resistance generated from longitudinal ribs (including the interface shear resistance and passive resistance from junctions) and the passive resistance that develops at the frontal surface of the transverse ribs. Ziegler and Timmers (2004) reported permanent deformations of transverse ribs of geogrid and welded steel samples after the pullout tests finished. Zhang et al. (2012) tracked the movements of sand particles in front of transverse ribs during pullout loading by using a microscope with a high-definition camera.

Transparent soils, such as that involving amorphous silica materials and pore fluids with a matching refractive index, have been recently to simulate classic geotechnical problems and to measure continuous spatial deformations in soils. Iskander (2010), and Ezzein and Bathurst (2011) introduced several types of transparent soils with their geotechnical properties and related optical measurement methods. Ezzein and Bathurst (2014) used a large-scale pullout test apparatus with transparent granular soil to evaluate the mobilization of the joints' displacement of geogrids at different pullout load levels. Ferreira and Zornberg (2015) conducted small-scale pullout tests with transparent granular soil and geogrids with markers to track the displacements in geogrid samples as well as the movement of soil particles during pullout loading. Chini et al. (2015) visualized the shearing failure of "transparent clay" using laboratory vane shear tests and penetrometer tests.

Uniaxial and biaxial geogrids have been widely utilized to reinforce geotechnical structures such as pavements and earth retaining structures. In recent years, geogrids with triangular apertures have been introduced into the market due to potential geometrical advantages compared with traditional uniaxial and biaxial geogrids. These include: (1) offering three principal directions of stiffness instead of one or two, (2) comparatively larger rib depth to facilitate confinement of soil particles, and (3) hexagonal junction shape with comparatively high junction strength and stiffness. Dong et al. (2011) conducted numerical evaluations to compare the tensile behavior of geogrids with rectangular apertures against that of geogrids with triangular apertures. They concluded that triaxial geogrid has far more uniform stress and strain distributions than the geogrid with rectangular aperture shape under tensile loading. Sun et al. (2014) indicated that the triaxial geogrid-stabilized pavement sections resulted in reductions in surface and subgrade permanent deformations as well as in a reduction of the horizontal pressures within the subgrade compared with unstabilized sections.

The pullout response of the triaxial geogrids can provide good insight into interaction mechanisms in spite of the relatively complex geometrical layouts of these geogrids. Transparent soils and related image processing techniques are used in this study to assess the deformation of the confined geogrids as well as the passive load transfer behavior of triaxial geogrids under pullout loading conditions.

2. MATERIALS AND TEST APPARARUS

2.1 Transparent Granular Soil

The solid material used in this study is crushed fused quartz, which has been previously used by Ferreira (2013). The particle-size distribution of this granular material is shown in Figure 1, and relevant geotechnical properties are summarized in Table 1.

The fluid used for transparent soil involves a mixture of two clear mineral oils: Puretol 7 and Paraflex HT4, which is similar to the mixture reported by Ezzein and Bathurst (2011) and Ferreira (2013). Puretol 7 has higher value of refractive index than the solid fused quartz, while Paraflex HT4 has lower value. Therefore, for the given volume ratio of these two liquids, the final combination is targeted at having the same refractive index as that of fused quartz. A

transparent soil sample (fused quartz fully saturated with the oil mixture) with an inserted biaxial geogrid is displayed in Figure 2.

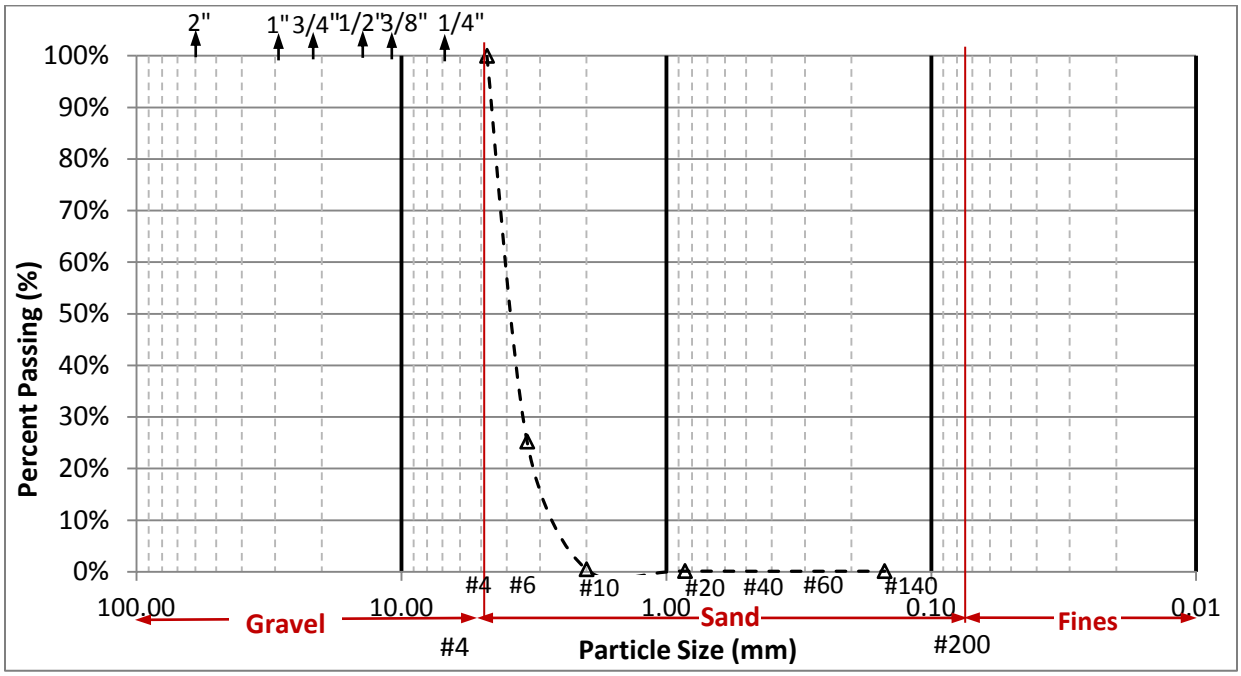

Figure 1. Particle-size distribution curve of fused quartz

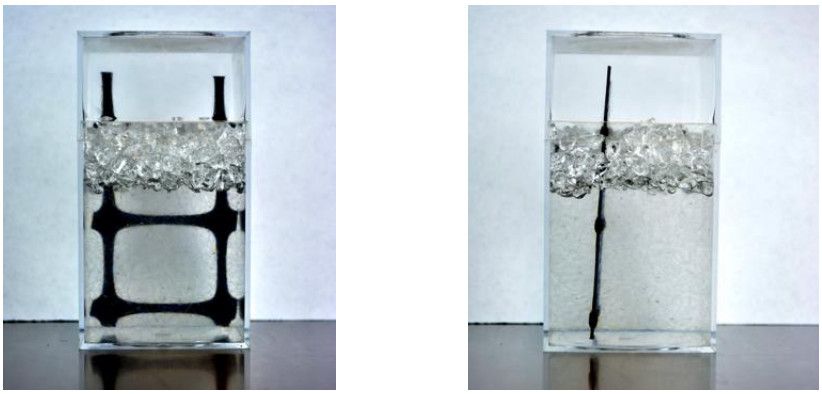

(a) (b)

Figure 2. (a) Frontal view and (b) side view of a transparent soil sample (fused quartz fully saturated with the oil mixture) with an inserted biaxial geogrid

Table 1. Geotechnical properties of fused quartz

Property	Test method	Value
Specific gravity (20°C)	Water Pycnometer Test (ASTM D854)	2.203
Maximum–index dry density	Vibratory Table Test (ASTM D4253)	1.336 (g/cm^3)
Minimum–index dry density	Vibratory Table Test (ASTM D4254)	1.203 (g/cm^3)
Friction angle (Dry)	Direct Shear Test (ASTM D3080)	45 (^{o})
Friction angle (Oil saturated, drained)	Direct Shear Test (ASTM D3080)	44 (^{o})

2.2 Triaxial Geogrid

The triaxial geogrid used in this study is manufactured from a punched polypropylene sheet, with the ribs oriented in three substantially equilateral directions. The geometrical characteristics of this geogrid are provided in Table 2.

Table 2. Geometrical properties of the triaxial geogrid (from manufacture's specification sheet)

Property	Longitudinal	Diagonal	General
Rib pitch	40 (mm)	40 (mm)	-
Mid-rib depth	1.6 (mm)	2.0 (mm)	-
Mid-rib width	1.3 (mm)	1.0 (mm)	-
Rib shape	-	-	Rectangular
Aperture shape	-	-	Triangular

2.3 Small-Scale Soil-Geosynthetic Interaction Test Setup

Figure 3 demonstrates the test apparatus used in this study. The loading system and the data acquisition system in this study are same as those reported by Ferreira (2013). High-definition cameras were used to capture deformations of the entire geogrid sample both in confined and unconfined portions of the sample. The sampling rate was 5 seconds. A loading displacement rate of 1 mm/min was applied during testing, and the frontal load and the captured images were synchronized by the data acquisition system. A light system composed of two 160 W photo studio soft boxes was used to provide uniform light on the transparent pullout box. The internal dimension of the transparent box is 300 mm × 250 mm × 150 mm (width × length × height), and the dimension of the triaxial geogrid in confined portion is about 211 mm × 231 mm (width × length).

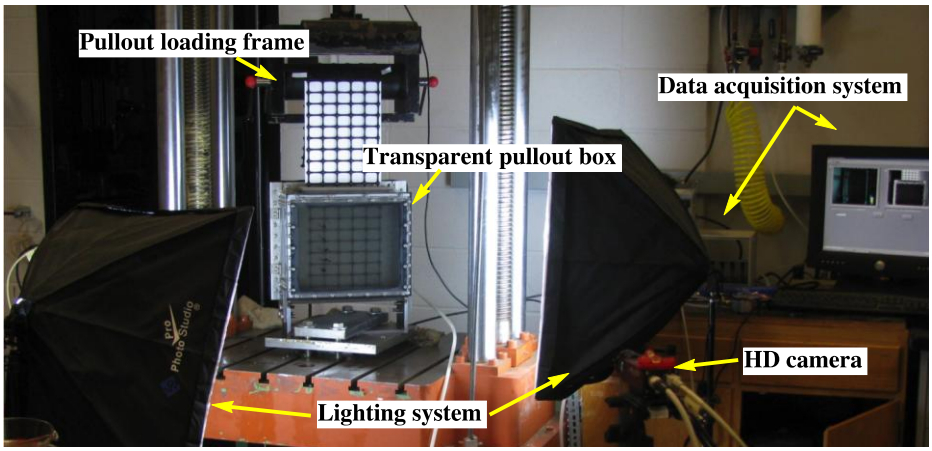

Figure 3. Transparent pullout test setup

3. IMAGE PROCESSING TECHNIQUES

Greyscale images captured during testing were used in this study for deformation tracking of the geogrid. An open source image processing tool package – ImageJ was utilized for image processing; further deformation capturing and data analysis were conducted using Mathematica codes and Excel spreadsheets. Particle Image Velocimetry (PIV) was used to observe the displacements of the junctions between longitudinal and transverse ribs of biaxial geogrids (Ezzein and Bathurst 2014), and some deformations of transverse ribs were captured by PIV with painting white markers on the rib surface (Ferreira 2013). PIV techniques were used to track paint markers. However, during the pullout testing, markers on the rib surface were peeled off due to a combination of straining, interface shear and oil saturation. These difficulties generated displacement tracking errors and also led to contamination of the transparency of the oil and fused quartz mixture. Ultimately, the technique described below was adopted.

Since the geometry of all the rib members of geogrid is symmetric, a series of image processing techniques were applied to generate the medial axis of all the rib members. Accordingly, the deflection can be visualized by tracking the shape of medial axis of all diagonal-rib members of the triaxial geogrid. The locations of intersections of the medial axes of ribs represent the location of rib junctions. Figure 4(a) and 4(b) show the cropped image frames for undeformed and deformed diagonal-rib elements. Figure 4(c) and 4(d) show the results generated by several image-processing algorisms (e.g. filtering, adjusting global and local brightness and contrast, subtracting background, binarization, etc.). Figure 4(e) and 4(f) have been obtained by removing pixels from the edges of ribs and junctions in binary images (Figure 4(c) and 4(d)) until they are reduced to single-pixel-wide shapes (also called topological skeletons).

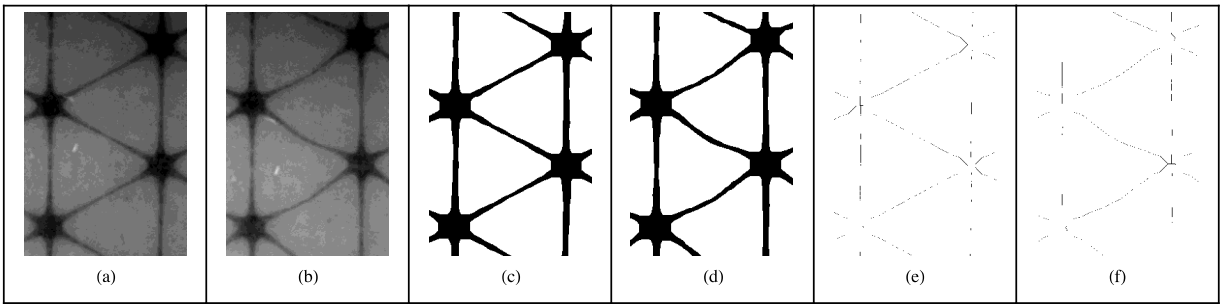

Figure 4. Key steps for image processing: cropped greyscale images for (a) undeformed rib-shape and (b) deformed rib-shape, and binary images for (c) undeformed rib-shape and (d) deformed rib-shape, and topological skeletons for (e) undeformed rib-shape and (f) deformed rib-shape

4. TEST RESULTS AND DISCUSSION

The results of one of the pullout tests involving transparent soil and triaxial geogrid are presented in this section. The test was conducted using an applied normal pressure of 27.6 kN/m^2, and the geogrid was pulled out along the cross-machine direction.

Figure 5(a) shows the frontal view of the transparent box at the beginning of the test. As can be seen in the figure, the confined section of the triaxial geogrid sample has 10 junctions and 9 diagonal ribs at different embedment depths. In this study, the total passive resistance at a given embedment depth was assumed to be developed uniformly by the diagonal-rib elements. Only the movement of junctions and deformations of diagonal ribs at the center section are discussed. The displacement mobilizations of all the junctions at different frontal force levels (the ratio of current pullout load to the peak pullout load) are presented in Figure 5(b). An exponential function was used by Ferreira (2013) to fit these displacement mobilizations.

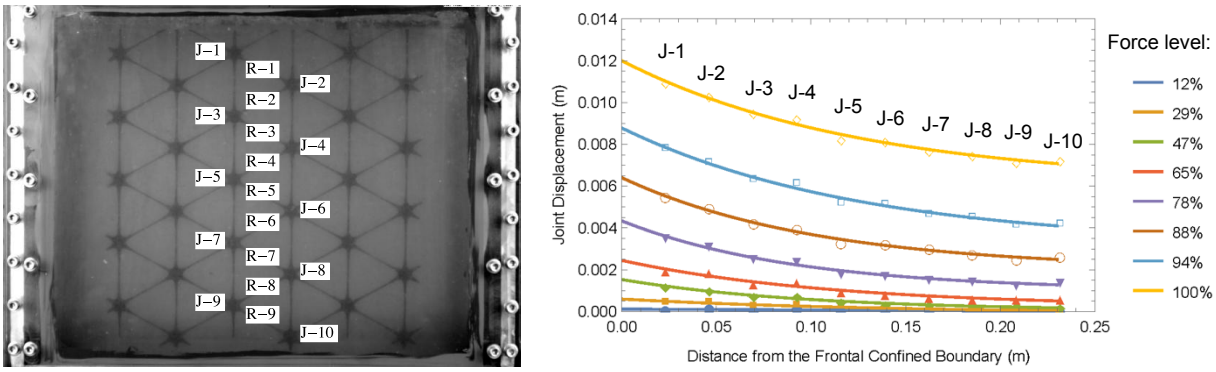

(a) (b)

Figure 5. (a) Frontal view of a pullout test and (b) junction-displacement profile of at different force levels

The deformations of the diagonal ribs were quantified by conducting the following steps: (1) discretizing the topological skeletons with a sequence of points; (2) locating these points in the Cartesian coordinate system; (3) the discretized diagonal ribs were rotated to horizontal (parallel to x axis) and the left ends of the ribs were shifted to the origin of Cartesian coordinate system.

An example of the application of these steps for one of the ribs (R-3 in Figure 5(a)) at the time of pullout failure is provided in Figure 6. Figure 6(a) shows a cropped image with topological skeletons, and 6(b) discretizes the topological skeletons with a sequence of red dots. The dots were located in the Cartesian coordinate system based on their pixel locations in the original image as shown in Figure 6(c). Figure 6(d) shows the dots-represented rib-shape after shifting and rotation, and 6(e) compares the un-deformed rib-shape and the deformed rib-shape of rib R-3 at pullout failure. As can be seen in Figure 6(e), the maximum deflection of this rib at stage of pullout failure is about 30.49 pixels, which corresponds to 2.04 mm (1 pixel = 6.68×10^{-2} mm), and its location along x-axis direction is at 19.45 mm (291.15 pixels) from the origin, and the project length of the rib along x-axis direction is 36.20 mm, so the eccentricity is about 1.35 mm to the right, and the ratio of eccentricity to the total project length of the rib along x-axis direction is 3.73%.

The angle between the deformed rib at the stage of pullout failure and the horizontal direction is considered to be the slope of the linear fitting line for the dots shown in Figure 6(c). This angle θ was used to rotate the dots in Figure 6(c) to horizontal as shown in Figure 6(d). Angle θ is shown in Figure 7(a), and the change of θ ($\Delta\theta$) at different load levels is provided in Figure 7(b). In Figure 7(b), it can be seen that $\Delta\theta$ increases with increasing frontal load. This may be due to the necking effect when the applied normal pressure was not high enough. However, the final value of $\Delta\theta$ is about 0.8°, which means the necking effect was comparatively small.

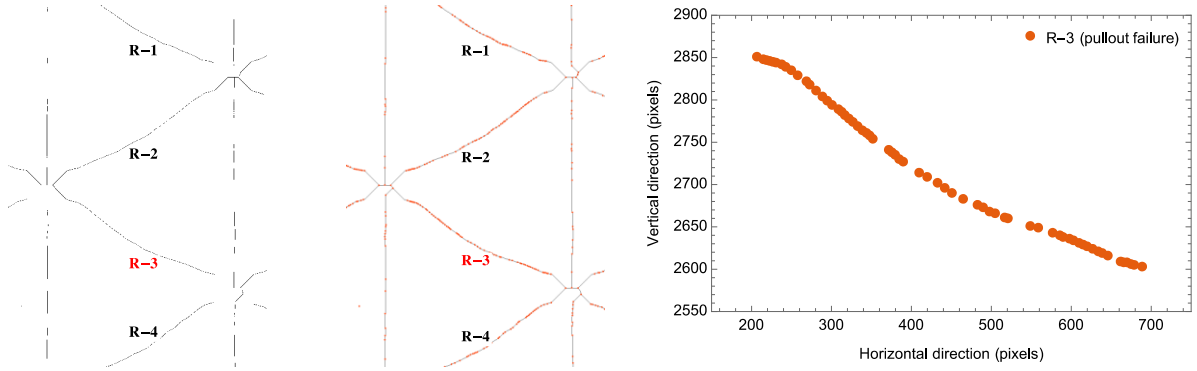

(a) (b) (c)

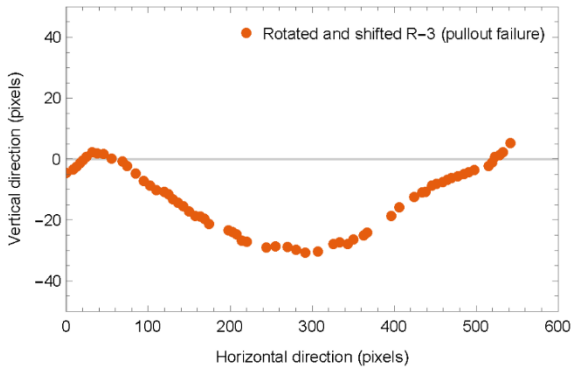

(d)

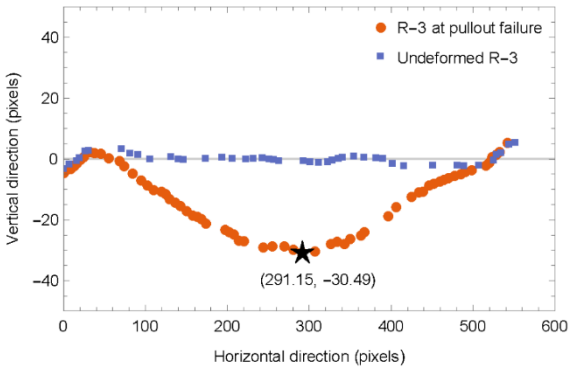

(e)

Figure 6. (a) A cropped image with topological skeletons, and (b) discretized topological skeletons with a sequence of red dots, and (c) dots located in the Cartesian coordinate system, and (d) the dots-represented rib-shape after shifting and rotation, and (e) a comparison between the un-deformed rib-shape and the deformed rib-shape at pullout failure

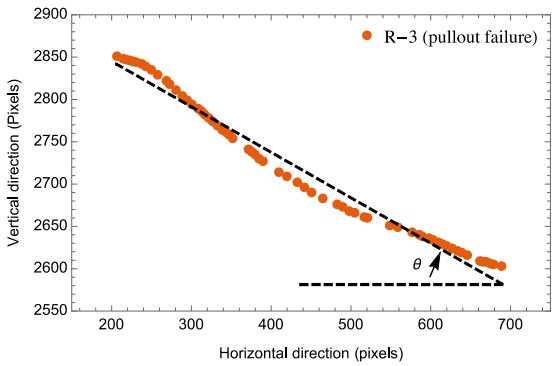

(a)

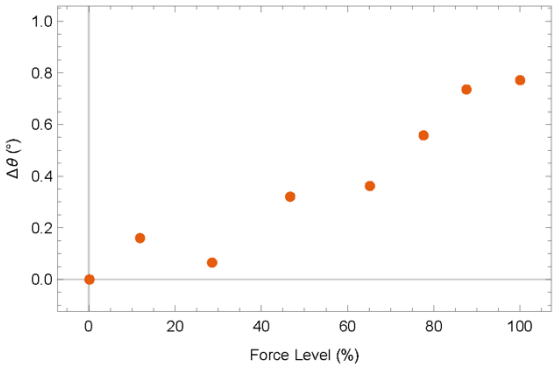

(b)

Figure 7. (a) The definition of the slope angle of the deformed rib-shape and (b) the variation of the change of this angle at different pullout force levels

The maximum deflections in rib R-3 at different load levels were obtained by applying the steps illustrated in Figure 6. Similar analyses were conducted for other ribs identified in Figure 5(a). Also, the average displacements of the two end junctions of all diagonal ribs (e.g. in Figure 5(a), J-3 and J-4 are the two junctions at the two ends of rib R-3) were calculated based on the data illustrated in Figure 5(b). The relationship between the average displacements and time (and also pullout force levels) is provided in Figure 8(a). The average junction displacements for each diagonal ribs were found to be comparatively small and did not change significantly when the pullout force levels were below 50%. The displacements then increased dramatically until pullout failure occurred. Figure 8(b) shows that the same relationship between the maximum deflections and the average junction displacements can be observed for all

diagonal ribs marked in Figure 5(a). A hyperbolic function was used to fit the data. This relationship may indicate the diagonal ribs at different embedment depths have similar boundary (fixity) conditions and loading conditions.

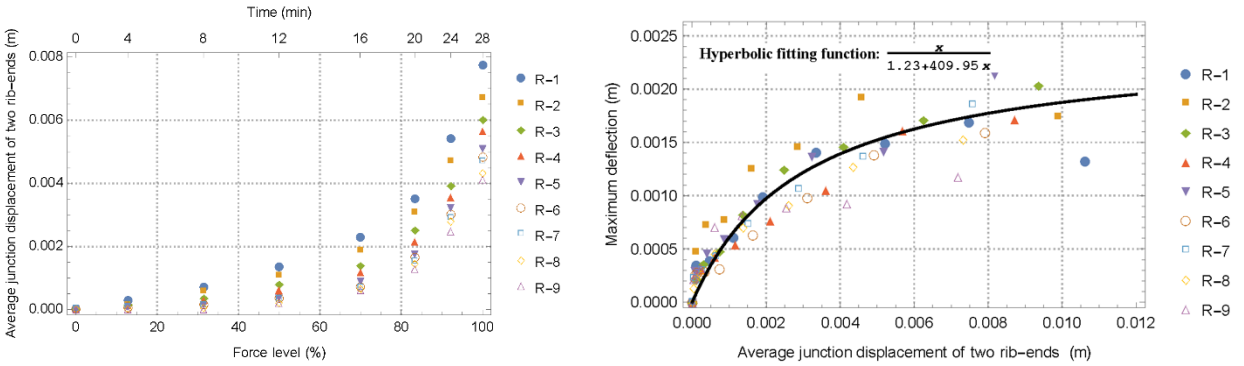

(a) (b)

Figure 8. (a) Variations of the average junction displacements of the two ends of diagonal ribs at different frontal load levels and (b) the relationship between the maximum deflections and these average junction displacements with a fitting function

In order to obtain a relationship between the deformation and the passive force of the diagonal ribs, an element-rib pullout test was conducted using the same normal pressure (27.6 kN/m^2) and loading speed (1 mm/min). In this test, only one layer of diagonal ribs was tested and all others were removed (Figure 9(a)). Clear PVC tubes were used to cover all longitudinal ribs and junctions to eliminate the development of interface friction. Slots at the two sides of tubes could leave enough spaces for the movement of diagonal ribs during testing. PVC tubes with smaller external diameter were inserted into the bottom of the bigger tubes to prevent the outer-tube deformation due to the applied normal stress. The frontal view of this special transparent pullout test is shown in Figure 9(b). With this approach, the longitudinal ribs and junctions can move freely inside of PVC tubes, and the measured frontal pullout load only resulted from the passive forces acted on the diagonal ribs.

The maximum deflections of the center rib at different frontal load levels were obtained by applying the steps described in Figure 6. Similarly, it was assumed that the total frontal pullout force (which is also equal to the total passive force in this case) is evenly distributed among all the diagonal ribs. Therefore, the relationship between the passive load and the maximum deflection of the diagonal rib can be plotted as shown in Figure 10. A parabola function was used to fitting the data, and we can see that the passive load is found to increase more at higher maximum deflections. This relationship could be an important basis for future analytic modeling for soil-geogrid load transfer mechanisms of intact geogrid samples.

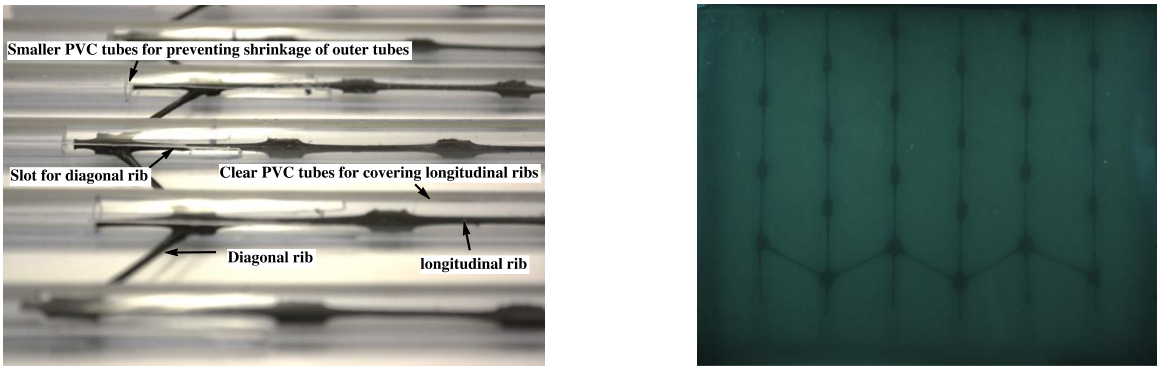

(a) (b)

Figure 9. (a) Close view of the design and (b) frontal view of the rib-element pullout test

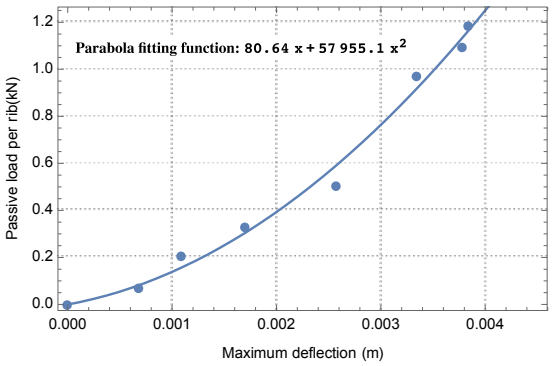

Figure 10. Relationship between the passive load and the maximum deflection of the diagonal rib

5. CONCLUSION

The use of transparent soil and related image processing techniques was found to be useful to investigate the load transfer mechanisms of triaxial geogrids. The tests involved small-scale pullout setups. The following conclusions can be drawn based on the testing results: (1) the image processing techniques adopted in this study was found to be adequate to capture the junction displacements and diagonal-rib deformations. (2) Visualization of the deformed shapes of the diagonal ribs during the pullout tests showed that the locations of maximum deflections are almost at the center of the ribs. (3) The angles defined by the deformed diagonal ribs and the horizontal were found to increase throughout the pullout tests. However, the change of these angles was found to be comparatively small (less than 1 degree). Consequently, the triangular aperture shape of the geogrid used in this study is deemed stable under pullout loading condition. (4) An unique relationship could be identified between the maximum deflections and the average junction displacements of two rib-ends for all diagonal ribs. This relationship indicates that the diagonal ribs at different embedment depths have similar boundary (fixity) conditions and loading conditions. (5) A nonlinear load-

deflection relationship of the diagonal rib was obtained from the results of a special rib-element pullout test, which could be an important basis for future analytic modeling for soil-geogrid load transfer mechanisms of intact geogrid samples.

ACKNOWLEDGEMENTS

The geosynthetics used in this study are provided by Tensar International Corporation. The authors gratefully acknowledge the valuable discussions with Dr. Mark Wayne. Dr. Julio Ferreira who finished the initial design of soil-geosynthetic interaction test setup also is gratefully acknowledged.

REFERENCES

Alagiyawanna, A. M. N., Sugimoto, M., Sato, S., and Toyota, H. (2001). Influence of longitudinal and transverse members on geogrid pullout behavior during deformation. *Geotextiles and geomembranes*, *19*(8), 483-507.

Chini, C., Wallace, J., Rutherford, C., and Peschel, J. (2015). Shearing Failure Visualization via Particle Tracking in Soft Clay Using a Transparent Soil. *Geotechnical Testing Journal*, *38*(5), 1-17.

Dong, Y. L., Han, J., and Bai, X. H. (2011). Numerical analysis of tensile behavior of geogrids with rectangular and triangular apertures. *Geotextiles and Geomembranes*, *29*(2), 83-91.

Ezzein, F. M., and Bathurst, R. J. (2011). A transparent sand for geotechnical laboratory modeling. *Geotechnical Testing Journal*, *34*(6), 1-6.

Ezzein, F. M., and Bathurst, R. J. (2014). A new approach to evaluate soil-geosynthetic interaction using a novel pullout test apparatus and transparent granular soil. *Geotextiles and Geomembranes*, *42*(3), 246-255.

Ferreira, J. A. Z. (2013). Evaluation of soil-geogrid interaction at different load levels using pullout tests and transparent soil (Doctoral dissertation). Retrieved from http://repositories.lib.utexas.edu/handle/2152/21153

Ferreira, J., and Zornberg, J. (2015). A Transparent Pullout Testing Device for 3D Evaluation of Soil–Geogrid Interaction. *Geotechnical Testing Journal*, *38*(5), 1-22.

Iskander, M. (2010). *Modelling with transparent soils: Visualizing soil structure interaction and multi phase flow, non-intrusively*. Springer Science and Business Media.

Ochiai, H., Otani, J., Hayashic, S., and Hirai, T. (1996). The pull-out resistance of geogrids in reinforced soil. *Geotextiles and Geomembranes*, *14*(1), 19-42.

Sieira, A. C. C., Gerscovich, D. M., and Sayão, A. S. (2009). Displacement and load transfer mechanisms of geogrids under pullout condition. *Geotextiles and Geomembranes*, *27*(4), 241-253.

Sun, X., Han, J., Wayne, M. H., Parsons, R. L., and Kwon, J. (2014). Experimental Study on Resilient Behavior of Triaxial Geogrid-Stabilized Unpaved Roads. In *Ground Improvement and Geosynthetics* (pp. 353-362). ASCE.

Teixeira, S. H., Bueno, B. S., and Zornberg, J. G. (2007). Pullout resistance of individual longitudinal and transverse geogrid ribs. Journal of geotechnical and geoenvironmental engineering, 133(1), 37-50.

Tran, V. D. H., Meguid, M. A., and Chouinard, L. E. (2013). A finite–discrete element framework for the 3D modeling of geogrid–soil interaction under pullout loading conditions. *Geotextiles and Geomembranes*, *37*, 1-9.

Wilson-Fahmy, R. F., and Koerner, R. M. (1993). Finite element modelling of soil-geogrid interaction with application to the behavior of geogrids in a pullout loading condition. *Geotextiles and geomembranes*, 12(5), 479-501.

Zhou, J., Chen, J. F., Xue, J. F., and Wang, J. Q. (2012). Micro-mechanism of the interaction between sand and geogrid transverse ribs. *Geosynthetics International*, *19*(6), 426-437.

Ziegler, M., and Timmers, V. (2004). A new approach to design geogrid reinforcement. In Proceedings of the 3rd European Geosynthetics Conference, Geotechnical Engineering with Geosynthetics.